ACS APPLIED MATERIALS & INTERFACES

www.acsami.org

Research Article

P-Type Doping of Mixed Tin−Lead Halide Perovskites Using Electron Transfer to Mo(tfd-COCF3)$_3$ and F$_4$TCNQ

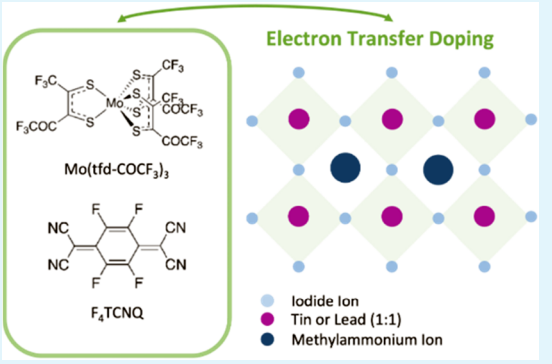
Migon Choi, Nelson Rivera, Steven P. Harvey, Chuanzhen Zhou, Sameera Pathiranage, Yadong Zhang, Stephen Barlow, Seth R. Marder, and David B. Mitzi*

Cite This: https://doi.org/10.1021/acsami.5c19800

Read Online

ACCESS | Metrics & More | Article Recommendations | Supporting Information

ABSTRACT: Mixed tin−lead halide perovskites are emerging as promising candidates to address the toxicity issues of lead-based perovskites and to provide additional bandgap tunability for optoelectronic applications. Electron-transfer doping offers a prospective pathway to modulate electronic properties of metal-halide perovskites, while not disturbing the underlying crystal structure. However, limited research exists comparing molecular dopants for these systems. Our study investigates the p-type electron-transfer doping of the mixed tin−lead halide perovskite $MAPb_{0.5}Sn_{0.5}I_3$ (MA = methylammonium) using a sequential deposition approach (perovskite film followed by dopant incorporation) and the molecular dopants F_4TCNQ and $Mo(tfd\text{-}COCF_3)_3$. Up to 3 orders of magnitude higher carrier density and up to 2 orders of magnitude greater conductivity are achieved relative to the undoped samples, with F_4TCNQ and $Mo(tfd\text{-}COCF_3)_3$ demonstrating similar doping efficiencies (associated with the ratio of mobile charges added to the number of dopant molecules incorporated) of 0.031(3) % and 0.024(3) %, respectively. Differences in the doping effectiveness for a given molarity doping solution likely follow from variations in dopant incorporation within the film during the spin coating deposition step.



KEYWORDS: *lead-free perovskites, additive engineering, electron transfer doping, charge carrier properties, doping efficiency*

Downloaded via DUKE UNIV on December 19, 2025 at 19:47:28 (UTC).
See https://pubs.acs.org/sharingguidelines for options on how to legitimately share published articles.

INTRODUCTION

Interest in lead (Pb)-free halide perovskite semiconductors has prompted the partial substitution of Pb with Sn to reduce Pb toxicity. 3D metal-halide perovskites have an ABX_3 structure, where A represents a monovalent organic or inorganic cation (e.g., $CH_3NH_3^+$, Cs^+), B is a divalent metal cation (e.g., Pb^{2+}, Sn^{2+}), and X is a halide anion (e.g., Br^-, I^-). Mixed Sn−Pb perovskites exhibit unusual properties for metal halides, notably narrow bandgaps (<1.3 eV),[1−3] leading to successful application in tandem solar cells as the low-gap absorber,[4] as well as in photodetectors and LEDs.[5,6] Mixed Sn−Pb perovskite solar cells have also reached power conversion efficiencies (PCE) > 23%,[7,8] comparable to Pb-based counterparts.[9]

To further enhance the performance and stability of halide perovskites, additive engineering has been extensively explored, which involves incorporating additional components beyond the targeted final stoichiometry to modify or improve material properties. For mixed Sn−Pb perovskites, additives have been introduced to suppress Sn oxidation,[10−14] control crystallization,[15−18] passivate surfaces and grain boundaries,[19−22] and tune charge-carrier lifetime and diffusion length.[23,24] Electrical doping, a subclass of additive engineering, allows for fine-tuning of charge-carrier density (i.e., shifting the Fermi level) and associated properties.[25,26] Investigating and controlling charge-carrier properties may also provide opportunities for optimizing the efficiency and stability of perovskite-based devices.[27] These properties, which include carrier density, mobility, and conductivity, directly influence prospective device performance by impacting electron/hole transport and photogenerated carrier recombination.[28,29] While perovskites are inherently challenging to electrically dope, given the high densities of potentially compensating defects, various strategies have been explored, including intrinsic or extrinsic defect doping, and electron-transfer doping.[30] In electron-transfer doping, the dopants are positioned on the surface of the grains or film, and not directly incorporated within the perovskite structure. As the dopants do not directly replace lattice ions, electron-transfer doping may reduce the tendency toward defect introduction through intrinsic/extrinsic doping. For instance, Euvrard et al. employed F_4TCNQ within the $MAPb_{0.5}Sn_{0.5}I_3$ system through electron-transfer doping and a simultaneous perovskite/dopant deposition process to dem-

Received: October 2, 2025
Revised: November 26, 2025
Accepted: December 2, 2025

© XXXX American Chemical Society

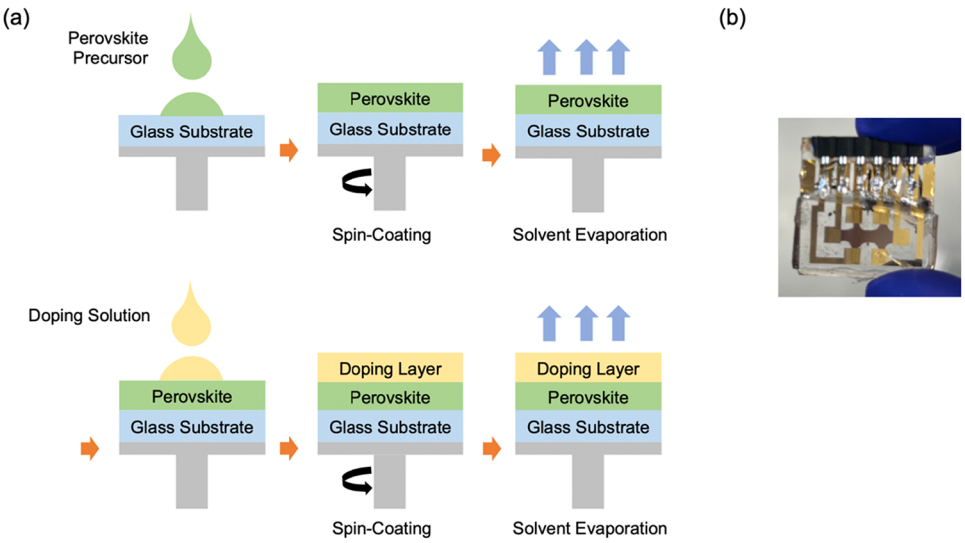


Figure 1. Schematic illustration of (a) film fabrication process. This process involves the steps of spin-coating, solvent evaporation, and annealing to prepare the perovskite film, followed by spin coating of the dopant. (b) Completed 6-terminal Hall bar device. The deposited films are precisely shaped into a Hall bar configuration by scratching (removing unwanted film) and electrode deposition, followed by encapsulation. All fabrication steps are carefully performed under a controlled nitrogen atmosphere to maintain material integrity.

onstrate enhanced carrier density and conductivity.[31] Noel et al. investigated the pure-Pb-based $FA_{0.85}MA_{0.15}Pb(I_{0.85}Br_{0.15})_3$ (FA = formamidinium), sequentially treated with Mo(tfd-$COCF_3)_3$ as a molecular dopant, achieving a 2-fold enhancement in conductivity compared to an undoped sample and an increased solar cell power conversion efficiency from 19.0 to 20.9%.[20]

Despite increasing interest in doping from the perovskite research community, understanding the comparative effectiveness of different p-type dopants in mixed Sn−Pb perovskites through electron-transfer doping remains in the early stages. In organic semiconductors, whether doping is performed simultaneously or sequentially significantly influences film morphology and doping efficiency.[32] Here, we demonstrate p-type charge-carrier modulation in mixed Sn−Pb perovskite films using a sequential deposition approach—i.e., depositing the perovskite film first followed by the dopant, to avoid the doping process possibly impacting perovskite film quality—and the molecular electron-transfer dopants F_4TCNQ (relatively shallower LUMO) and Mo(tfd-$COCF_3)_3$ (deeper LUMO, i.e., stronger oxidant). Our aims are 3-fold: (1) to prospectively enhance charge-carrier tunability and options for doping, (2) to characterize the morphology and dopant behavior within the thin films, and (3) to conduct a comparative analysis of the two dopants. This study contributes to the additive engineering field by demonstrating how molecular dopants like F_4TCNQ and Mo(tfd-$COCF_3)_3$ effectively tune charge-carrier properties, as well as by providing insights into p-type doping strategies for mixed Sn−Pb perovskites toward achieving higher device optoelectronic performance and stability.

RESULTS AND DISCUSSION

Perovskite Film Fabrication And Sequential Deposition Electron-transfer Doping. Before film fabrication, the quality of dopant starting materials was verified by checking the UV−vis peaks against established literature values, ensuring the integrity and consistency of the dopants[33,34] (Figure S1). The fabrication process starts with depositing the $MAPb_{0.5}Sn_{0.5}I_3$ precursor solution onto a glass substrate through spin-coating (Figure 1a; see Experimental Section for details). Premade perovskite films were used to reduce the likelihood of varying film morphology with dopant incorporation. After the perovskite spin-coating process, 1×10^{-3} M solutions of F_4TCNQ or Mo(tfd-$COCF_3)_3$ in chloroform were spin-coated onto the perovskite films. For the undoped sample, a pristine (no dopant added) chloroform solvent was spin-coated onto the film surface to better match the process used for the dopant-included solutions. Given the susceptibility of tin to oxidize ($Sn^{2+} \rightarrow Sn^{4+}$), which can substantially affect electrical properties (especially doping levels), all fabrication steps were carried out in a glovebox under nitrogen flow to prevent oxidation. The final step involves creating 6-terminal Hall bar devices from the films (Figure 1b).

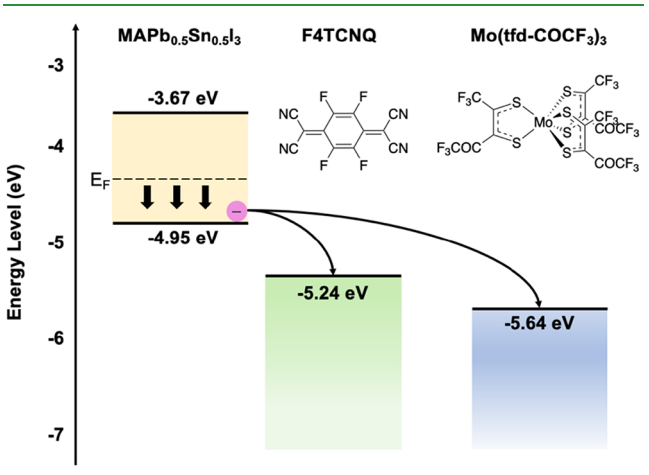


Figure 2. Estimated energy-level alignment showing schematic electron-transfer doping in mixed Sn−Pb perovskite with p-type dopants,[36,37] along with F_4TCNQ and Mo(tfd-$COCF_3)_3$ structures. Both the valence band maximum and conduction band minimum are shown for the perovskite, while the LUMO is shown for the two molecular dopants.

https://doi.org/10.1021/acsami.5c19800
ACS Appl. Mater. Interfaces XXXX, XXX, XXX−XXX

Energy-level alignment—i.e., involving the HOMO of the perovskite and the LUMO of the dopant—represents a critical factor in the doping process. When the HOMO (or valence band edge) of the perovskite lies higher than the dopant LUMO, electrons may transfer from the perovskite to the dopant, leading to p-type doping and a lowering of the Fermi level for the perovskite film. Specifically, the HOMO of $MAPb_{0.5}Sn_{0.5}I_3$ lies at −4.95 eV,[35] which can be compared to the estimated LUMO levels for F_4TCNQ and Mo(tfd-$COCF_3)_3$ of −5.24 and −5.64 eV, respectively. LUMO values were estimated from the electron affinities (EA) of the dopants: for F_4TCNQ determined via inverse photoemission spectroscopy (IPES), and for Mo(tfd-$COCF_3)_3$ determined using electrochemical comparison to a related compound for which IPES was measured.[36,37] The EA values represent the energy released on addition of an electron to the LUMO—i.e., if one assumes an extension of Koopmans' theorem, EA = $-E_{LUMO}$, where E_{LUMO} is the LUMO energy level relative to the vacuum (Figure 2). The HOMO and LUMO levels are typically estimated for neat films of the dopant molecules and may differ in real-world conditions—i.e., when incorporated within other materials and at interfaces. Neglecting these effects, since Mo(tfd-$COCF_3)_3$ has a lower LUMO than F_4TCNQ, it might be expected that Mo(tfd-$COCF_3)_3$ could exhibit higher doping efficiency.

Morphologies and Crystallinities of Perovskite Films. Powder X-ray diffraction (XRD) (Figure 3) and scanning electron microscopy (SEM) (Figure 4) were conducted for phase identification and film morphology investigation, respectively. Notably, sharp X-ray diffraction peaks appear at 19.98 and 40.70°, corresponding to reflections from the (110) and (220) planes of the perovskite structure, respectively. These observations point to a [110] preferred crystallographic orientation, consistent with observations from the literature.[38] Peak patterns are consistent across all samples, indicating that the application of the dopant does not impact the film crystal structure or phase purity. The SEM images show a consistent apparent grain size (based on breaks or grooves seen in the SEM images) of ∼10 μm across all samples. Features attributed to aggregates are observed on the surfaces of the F_4TCNQ-doped films, the formation of which during solution deposition might be due to the planar structure and relatively low solubility of F_4TCNQ. Such morphological features are critical as they can influence film electronic properties—e.g., act as trap sites, or disrupt the continuous charge-transport pathways, potentially leading to increased charge-carrier recombination or scattering.[39−41]

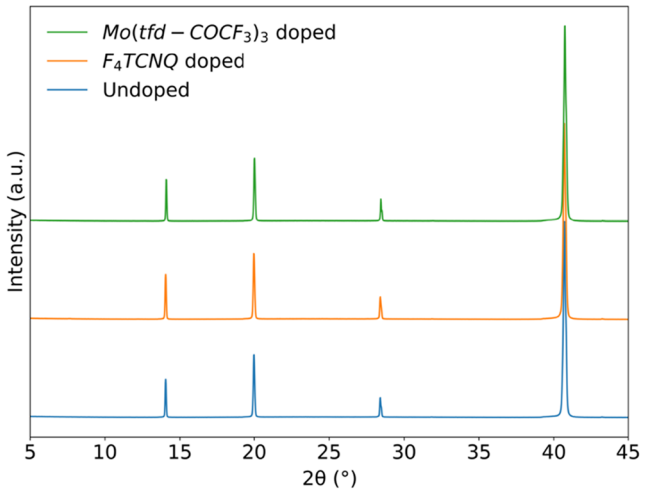


Figure 3. X-ray diffraction (XRD) of undoped, 1 × 10^{-3} M F_4TCNQ-doped, and 1 × 10^{-3} M Mo(tfd-$COCF_3)_3$-doped $MAPb_{0.5}Sn_{0.5}I_3$ films.

Electronic Properties of Doped Perovskite Films. Figure 5 compares the charge-carrier densities, conductivities, and mobilities among the undoped and doped perovskite films, through dark Hall measurement (Figures S2−S4). The film thicknesses, critical for associated calculations, are determined using profilometer measurements (Figure S5). To ensure precision in our measurements and to reduce the influence of contact resistance, the study employed a 4-point probe approach within the 6-terminal Hall bar configuration (see Experimental Section for more details). The undoped $MAPb_{0.5}Sn_{0.5}I_3$ films exhibit carrier densities ranging from ∼10^{14} to 10^{15} cm^{-3}. This range is significantly lower—i.e., by one to 3 orders of magnitude—than for films doped with 1 × 10^{-3} M F_4TCNQ and 1 × 10^{-3} M Mo(tfd-$COCF_3)_3$ (Figure 5a). Such a substantial increase in carrier density in the doped samples indicates that relatively effective p-type doping can be achieved by deposition of either Mo(tfd-$COCF_3)_3$ or F_4TCNQ onto the perovskite film surfaces. Although the measurement duration in this study (∼1200 s) was not specifically designed to capture persistent photoconductivity (PPC), recent findings by Euvrard et al. suggest that extending measurements to longer time scales (∼100 h) could provide valuable insights into whether PPC influences carrier density, conductivity, and mobility in doped perovskite films.[42]

While the carrier densities increase from undoped films to Mo(tfd-$COCF_3)_3$-doped films to F_4TCNQ-doped films, the mobility values decrease (Figure 5b). Previous studies have pointed out that inverse relationships of this type could originate from phonon scattering, carrier−carrier scattering, and Coulomb scattering, due to enhanced interaction among phonons, carriers, and ionized impurities.[43−45] The conductivity values of the undoped $MAPb_{0.5}Sn_{0.5}I_3$ films range from 10^{-3} to 10^{-4} S·cm^{-1} (Figure 5c), consistent with, and in

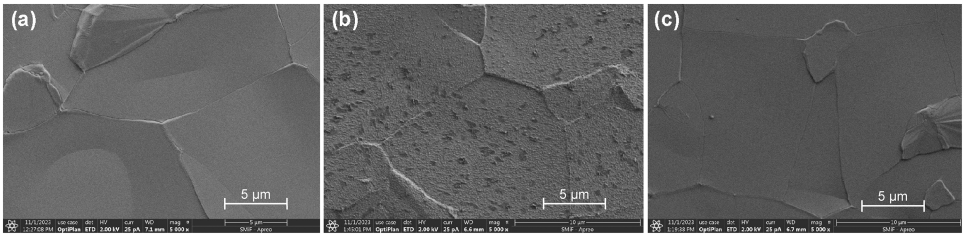


Figure 4. SEM images of (a) undoped, (b) 1 × 10^{-3} M F_4TCNQ-doped, and (c) 1 × 10^{-3} M Mo(tfd-$COCF_3)_3$-doped $MAPb_{0.5}Sn_{0.5}I_3$ films.

https://doi.org/10.1021/acsami.5c19800
ACS Appl. Mater. Interfaces XXXX, XXX, XXX−XXX

some cases slightly lower than, those reported in the literature.[46] However, the doped samples demonstrate conductivities enhanced by one and 2 orders of magnitude, respectively, for the 1×10^{-3} M Mo(tfd-$COCF_3$)$_3$ and 1×10^{-3} M F_4TCNQ films. These enhancements in electrical conductivity further confirm the efficacy of the doping process, aligning with the increases in carrier density and the associated modifications to the electronic structure of the perovskite material.

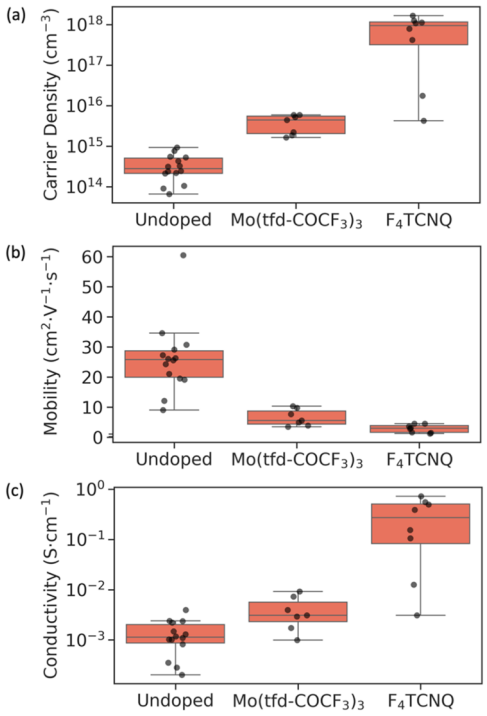


Figure 5. Dark Hall measurements (including statistics over multiple measured samples) for (a) carrier density, (b) Hall mobility, and (c) conductivity as a function of doping type. The box plots show the distribution of carrier densities, mobilities, and conductivities for different doping materials, with the boxes representing the middle 50% of the data, the whiskers indicating the range within 1.5 times the interquartile range, and any points beyond the whiskers as potential outliers.

Dopant Distribution in Films. The spatial dopant distribution within the perovskite films was investigated through time-of-flight secondary ion mass spectroscopy (TOF-SIMS) analysis (see Experimental Section for details). 2D imaging and 3D tomography were conducted on F_4TCNQ and Mo(tfd-$COCF_3$)$_3$-doped samples (Figure 6). In the summation intensity 2D images (Figure 6a,b), we identify the fluorine (F) and molybdenum (Mo) signals coming from F_4TCNQ and Mo(tfd-$COCF_3$)$_3$ molecules, respectively. Higher signal intensities are observed from the F_4TCNQ-doped sample, in part due to the higher ion probability for F (which can substantially influence the perceived dopant density distribution). Localized enhanced signals were detected at the surface of the F_4TCNQ-doped sample (Figure 6a), consistent with the presence of aggregates of F_4TCNQ, as previously noted from the SEM analysis. SEM images and 2D TOF-SIMS imaging do not reveal evidence of aggregation for the Mo(tfd-$COCF_3$)$_3$ dopant within the associated films. The 3D tomography renderings provide further insights into the depth profiles of the dopants (Figure 6c,d). For both dopants, the 3D TOF-SIMS profiles indicate a higher dopant concentration at the surface—not a surprising result, given that the dopant is spin coated on top of the perovskite film. TOF-SIMS results reflect that both F_4TCNQ and Mo(tfd-$COCF_3$)$_3$ contribute to the fluorine signal, with the Cs_2F^+ trace highlighting dopant incorporation (Figure S6). Given the lower overall Mo(tfd-$COCF_3$)$_3$ dopant incorporation, it is more challenging to assess the associated detailed depth distribution (Figure S7). A small background fluorine signal was observed in the TOF-SIMS analysis of the undoped $MAPb_{0.5}Sn_{0.5}I_3$ sample (Figure S8). However, a F signal was also present in the bare glass substrate, suggesting that the signal may originate from the substrate rather than the perovskite film itself. This F intensity was also several orders of magnitude lower than that of the doped samples (i.e., compare Figures S8 and S9). As such, this background fluorine was considered negligible and did not impact the conclusions of the study.

Assessment of Doping Efficiency in Perovskite Films. Semiquantitative analysis is conducted to calculate the doping efficiencies of Mo(tfd-$COCF_3$)$_3$ and F_4TCNQ in perovskite films using inductively coupled plasma mass spectroscopy (ICP-MS) and TOF-SIMS (Tables S1 and S2). In general, TOF-SIMS cannot be considered quantitative without employing a standard. The secondary ion yield of doped materials, in this case F^-, could be affected by the matrix (Figure S9). The secondary ion intensities of matrix ions, including SnI_2^- and PbI_2^-, are similar for the undoped and Mo(tfd-$COCF_3$)$_3$ samples, suggesting the doping level is low and does not affect the matrix. However, the secondary ion intensity of the matrix ions is somewhat lower for the F_4TCNQ sample compared to the undoped sample. Prospectively, this lower intensity might arise from a higher dopant concentration , which changes the matrix composition enough to alter the TOF-SIMS ionization probability. However, we compare the aggregate intensity values for the films, which have the same thickness (Figure S5), and observe similar relative matrix signals (Table S2). From PXRD analysis, we know that the application of the dopant does not impact the structure of the matrix ($MAPb_{0.5}Sn_{0.5}I_3$) (Figure 3). Therefore, the altered matrix signal likely arises due to the significant increase in the surface roughness for the F_4TCNQ sample, as evidenced by the increased sputter time needed to reach the similar intensity of the substrate signal (Figure S9). Furthermore, when we integrate the matrix signal from the film region, including both the main region of the film and the interface, we notice that the cumulative ion counts from the F_4TCNQ-doped matrix are comparable to those from the Mo(tfd-$COCF_3$)$_3$-doped matrix (Table S2), for profiles of the same thickness films (Figure S5). Thus, all the current calculations assume that we are using the integrated value and that different substrates did not affect F ion yield.

The evaluation of doping efficiencies for 1×10^{-3} M F_4TCNQ and Mo(tfd-$COCF_3$)$_3$-doped perovskite films follows from eq 1 (see Supporting Information). The numerator of this ratio represents the number of carriers introduced by the doping process and is derived by calculating the difference in the average carrier density between the undoped and the doped samples from the Hall measurements. ICP-MS was employed to determine the Mo concentration for the Mo(tfd-$COCF_3$)$_3$-doped $MAPb_{0.5}Sn_{0.5}I_3$ films (Table S1). Given the specific dimensions of the film and the known stoichiometry of Pb and Sn atoms, the total count of Mo atoms

https://doi.org/10.1021/acsami.5c19800
ACS Appl. Mater. Interfaces XXXX, XXX, XXX−XXX

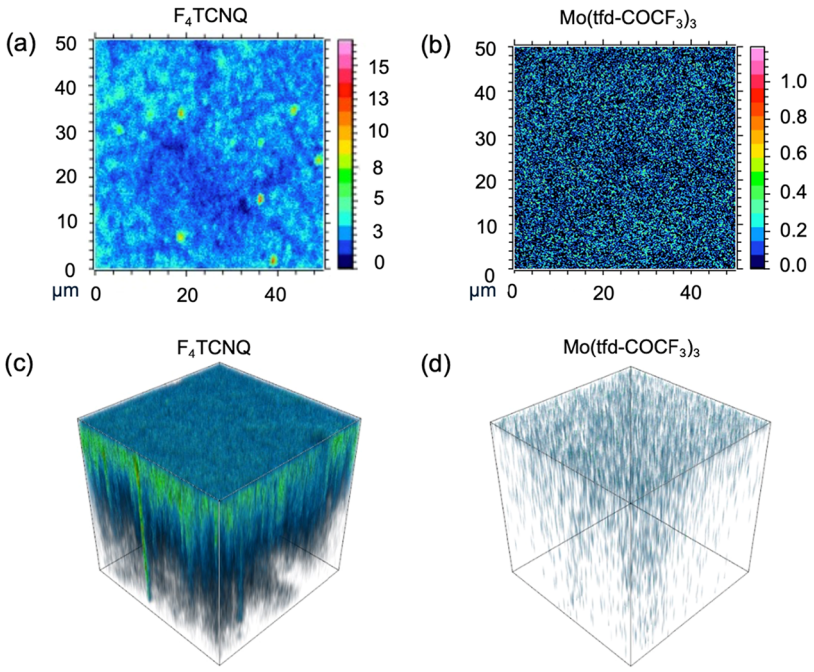


Figure 6. TOF-SIMS 2D images of (a) F signal from 1×10^{-3} M F_4TCNQ-doped and (b) Mo signal from 1×10^{-3} M $Mo(tfd\text{-}COCF_3)_3$-doped $MAPb_{0.5}Sn_{0.5}I_3$ films. Each image is 50 μm × 50 μm and the color scale for each image shows the signal intensity in counts/pixel. TOF-SIMS 3D tomography rendering, showing the signal coming from (c) the F signals, and (d) Mo signals. Each 3D reconstruction is 50 × 50 × film thickness μm^3.

was estimated as 1.56×10^{15} atoms, which translates to an equivalent number of the corresponding dopant molecules. For fluorine quantification, TOF-SIMS was utilized (given the challenges of assessing F content with ICP), taking advantage of the known ratio from the $Mo(tfd\text{-}COCF_3)_3$ sample (i.e., from the ICP-MS measurement), which contains 18 fluorine atoms per dopant molecule. The F content in the Mo sample is thereby considered as $\sim 2.81 \times 10^{16}$ atoms. Subsequently, by measuring the relative F signals from both dopant samples, and with a calculated F signal ratio of 40.2, the F_4TCNQ sample was determined to contain roughly 1.13×10^{18} F atoms (Table S2). Given that each F_4TCNQ molecule contains four F atoms, this correlates to $\sim 2.83 \times 10^{17}$ F_4TCNQ molecules present within or on the film.

$$\text{doping efficiency (\%)} = \frac{\text{the number of carriers generated from doping}}{\text{the number of dopant molecules incorporated}} \times 100 \quad (1)$$

Employing the above quantifications and eq 1, the results indicate a doping efficiency of 0.024(3) % for $Mo(tfd\text{-}COCF_3)_3$ and 0.031(3) % for F_4TCNQ. We estimated measurement errors of ~5% for ICP-MS and ~10% for TOF-SIMS measurements, though there may be greater uncertainty arising from the experimental procedures themselves (e.g., due to film surface roughness and inhomogeneity). Given the experimental uncertainties and the limits of measurement accuracy, the doping efficiency values are considered to fall within the same range. The above-reported modest efficiencies may reflect that molecular dopants in hybrid perovskites are primarily localized at grain boundaries, where limited interfacial charge transfer and dopant aggregation could constrain effective carrier generation.[47,48] While quantitative evaluations of molecular p-doping efficiency in mixed Sn−Pb perovskites remain scarce, the present analysis provides a useful methodological benchmark for future comparison.[31]

Although we previously mentioned the hypothesis that $Mo(tfd\text{-}COCF_3)_3$ might exhibit higher doping efficiency than F_4TCNQ due to its lower LUMO, the similar observed doping efficiencies may relate to differences in how the molecules interact with the perovskite surface (given different chemical functional groups for the two dopants). Further, we can surmise that the differences between F_4TCNQ and $Mo(tfd\text{-}COCF_3)_3$-doped films, prepared using the same molarity dopant solutions, in terms of measured carrier densities, mobilities, and conductivities, may predominantly arise due to differences in incorporation of the two types of dopants into the films, rather than to differences in inherent doping efficiencies for the two dopants. Such differences in interaction may stem from variations in molecular size, steric constraints, and Lewis basicity of the dopant functional groups, which could influence interfacial charge transfer and local dielectric stabilization at the perovskite surface.[49,50]

The aggregation of F_4TCNQ on the perovskite layer compared to $Mo(tfd\text{-}COCF_3)_3$ after a spin-coating process (despite the similar molarity in the deposition solution) may arise from differences in molecular structure and substrate interactions. As the spin-coating process advances, the solvent evaporation rate plays a critical role, emphasizing the significance of the residual molecular structure on the surface—i.e., the molecular properties dictate the adsorption dynamics. Differences in dopant incorporation can therefore arise from dopant solubility and molecular structure. First, F_4TCNQ has a solubility of approximately 0.5 mg/mL (corresponding to 2×10^{-3} M), much lower than for $Mo(tfd\text{-}COCF_3)_3$, which has a solubility of ~30 mg/mL (ca. 3×10^{-2} M).[51,34] The concentration of the F_4TCNQ doping solution (1×10^{-3} M) approaching the solubility limit may

https://doi.org/10.1021/acsami.5c19800
ACS Appl. Mater. Interfaces XXXX, XXX, XXX−XXX

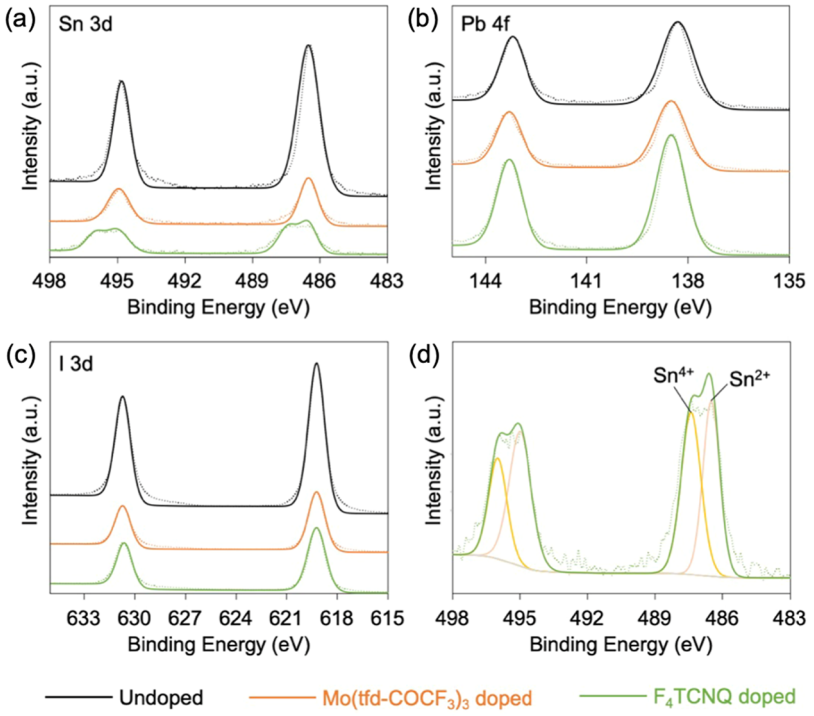


Figure 7. High-resolution X-ray photoelectron spectroscopy (XPS) scans of $MAPb_{0.5}Sn_{0.5}I_3$ thin films: (a) Sn 3d, (b) Pb 4f, and (c) I 3d spectra for exemplary undoped, F_4TCNQ-doped, and $Mo(tfd\text{-}COCF_3)_3$-doped samples; (d) Deconvolution of peaks within the Sn 3d spectrum of F_4TCNQ-doped $MAPb_{0.5}Sn_{0.5}I_3$ films.

readily contribute to aggregate formation on the film surface. Second, planar molecules like F_4TCNQ with strong electron-accepting character are more likely to closely pack on the perovskite surface relative to bulkier molecules that extend in a 3D fashion. This behavior agrees with observations of similar organic semiconductors as reported in Dixon et al.[40] In addition, factors such as $\pi-\pi$ stacking and steric shielding behavior may further promote aggregation, consistent with prior observations of F_4TCNQ clustering on organic semiconductor surfaces.[47]

Photoelectron Spectroscopy Evaluation of Core Levels. X-ray photoelectron spectroscopy (XPS) was employed to further explore the molecular doping process. Full XPS survey spectra are provided in Figure S10. High-resolution scans of Pb 4f, Sn 3d, and I 3d (Figure 7) show that Sn remains predominantly in the +2 oxidation state (Sn^{2+}) for both the undoped (avg. 486.53 eV) and the $Mo(tfd\text{-}COCF_3)_3$-doped (avg. 486.54 eV) samples, consistent with literature values for Sn^{2+}, whereas Sn^{4+} is typically observed at ~487.4 eV ($Sn\ 3d_{5/2}$).[52,53] These average values represent the mean across several experimental runs (see Figure S11 for intra- and intersample variability and Table S3 for mean values and standard deviations). In contrast, the F_4TCNQ-doped sample typically (in two of the three films examined; see Figure S11) exhibits a clear splitting of the Sn $3d_{5/2}$ peak into two components at 486.47 ± 0.13 and 487.51 ± 0.13 eV, corresponding to a separation of ~1.0 eV. This separation agrees with the expected difference between Sn^{2+} and Sn^{4+} oxidation states in octahedrally coordinated tin halides (e.g., ~0.9 eV between SnF_2 and K_2SnF_6[54]), thus suggesting localized oxidation of Sn^{2+} to Sn^{4+}. The presence of Sn^{4+} in Sn-based hybrid perovskites has typically been associated with enhanced hole concentration (i.e., doping).[55]

The absence of a Sn^{4+} feature in all but the F_4TCNQ-doped sample indicates that the films do not, in general, experience oxidation from the ambient environment (due to sample handling protocols, which target avoiding air exposure). The emergence of Sn^{4+} only in the F_4TCNQ-doped sample highlights a chemically specific interaction. The difference relative to the $Mo(tfd\text{-}COCF_3)_3$-doped films may arise from the small size and planar geometry of F_4TCNQ, which allows it to approach Sn^{2+} centers and act as a Lewis base. This interaction is consistent with prior observations that cyanocarbon radicals such as $TCNE^{\bullet-}$ and $TCNQ^{\bullet-}$ can coordinate and stabilize Sn^{4+} species.[56] $Mo(tfd\text{-}COCF_3)_3$, in contrast, is larger, less diffusive, and a less effective Lewis base, and thus may not induce a measurable local chemical change. The higher concentration of F_4TCNQ in the F_4TCNQ-doped film (relative to $Mo(tfd\text{-}COCF_3)_3$ in the corresponding doped sample) may also contribute to the different expression of the Sn^{4+} feature in the examined films. Pb 4f, I 3d, and Sn^{2+} (Sn 3d) components also remain unchanged within the measurement uncertainty (standard deviation ≈ 0.1 − 0.25 eV; See Figure Table S3). Notably, as all measured core levels are referenced to the C 1s peak, absolute Fermi level shifts between doped and undoped samples cannot be reliably assessed using the XPS data. Accordingly, our conclusions are limited to chemical-state information.

CONCLUSIONS

In this work, we achieve successful p-type doping in mixed-Sn/Pb perovskite films through electron-transfer doping using a sequential deposition approach. F_4TCNQ-doped $MAPb_{0.5}Sn_{0.5}I_3$ films show aggregation on the surface, and higher carrier density and conductivity compared to those involving $Mo(tfd\text{-}COCF_3)_3$, given the same molarity of dopant solutions. However, both F_4TCNQ and $Mo(tfd\text{-}COCF_3)_3$

https://doi.org/10.1021/acsami.5c19800
ACS Appl. Mater. Interfaces XXXX, XXX, XXX−XXX

exhibit similar doping efficiencies, once differences in film dopant incorporation during the sequential deposition process (likely due to differences in dopant molecular configuration and functionalization) are considered. The current results highlight the importance of optimizing interfacial interactions between dopant and the perovskite film. Future directions include investigating different ratios of Pb and Sn in perovskites, analyzing defect density variations as a function of surface doping, and incorporating p-type doped perovskite films into photovoltaic devices to study their performance and stability. These studies will provide a deeper understanding of dopant-induced effects and guide the development of efficient and stable perovskite-based optoelectronic devices.

EXPERIMENTAL SECTION

Perovskite Film and Hall Bar Fabrication. To prepare the perovskite precursor solutions, methylammonium iodide (MAI, Dyesol), lead iodide (PbI_2, 99.99%, TCI chemicals) and tin(II) iodide (SnI_2, anhydrous beads, 99.99%, Sigma-Aldrich) were dissolved in *N*,*N*-dimethylformamide (DMF, 99.8%, anhydrous, Sigma-Aldrich) and dimethyl sulfoxide (DMSO, 99.9%, anhydrous, Sigma-Aldrich) with an 85:15 volume ratio at a concentration of 1.25 M. The perovskite precursor solutions were stirred at room temperature for 1 h for all film preparations. Glass substrates (2 cm × 2 cm) were sonicated in deionized water, acetone, and isopropanol for 10 min each followed by a 10 min plasma etch treatment. The solutions were filtered using hydrophilic PTFE 0.2 μm filters and spin-coated (without using an antisolvent) within 30 min of solution preparation. 53 μL of perovskite precursor solution was deposited onto a glass substrate and spin-coated at 5000 rpm for 100 s followed by an annealing step on a hot plate at 90 °C for 20 min.

After the perovskite layer was deposited, the doping layer was spin-coated on top. For doping solutions, 2,3,5,6-tetrafluoro-7,7,8,8-tetracyanoquinodimethane (F_4TCNQ, >98%, TCI chemicals) and molybdenum tris[1-(trifluoroethanoyl)-2-(trifluoromethyl)ethane-1,2-dithiolene] ($Mo(tfd\text{-}COCF_3)_3$, synthesized as previously described)[57] were dissolved in chloroform (>99.8%, Sigma-Aldrich) at $1.0(2) \times 10^{-3}$ M concentration. The solutions were stirred at 60 °C for 1 h and cooled to ambient temperature. 100 μL of doping solutions (1.0×10^{-3} M of F_4TCNQ and $Mo(tfd\text{-}COCF_3)_3$ in chloroform) were deposited onto each perovskite film within 30 min of solution preparation. Spin-coating was at 2000 rpm for 45 s followed by annealing at 100 °C for 10 min. The undoped sample was subjected to the same annealing process after spin coating with a chloroform solvent without dopant.

The Hall bars had six terminals with active area dimensions of width × length = 2 mm × 4 mm and were patterned using a mask and a razor blade to remove the surrounding film (Figure 1b). Gold electrodes (100 nm) were deposited through a shadow mask by thermal evaporation using an Angstrom EvoVac evaporator operating at a base pressure below 2×10^{-6} Torr. The Hall bars were encapsulated with glass using epoxy (from Ellsworth) on the perimeter only. The entire fabrication process, from perovskite film deposition to encapsulation, was conducted in a nitrogen-filled glovebox.

X-ray Diffraction/SEM Characterizations. X-ray diffraction (XRD) measurements were conducted using a Panalytical Empyrean powder diffractometer with Cu Kα X-ray source and 45 kV/40 mA operating conditions. Scanning electron microscope (SEM) imaging was used to obtain film morphology measurements, using an Apreo S by ThermoFisher Scientific operated at 2 kV and 25 pA.

ICP Spectroscopy. Thin films were dissolved in 2 mL of trace metal grade hydrochloric acid and 1 mL of nitric acid, then diluted to a 20 mL volume with 18.2 MΩ water. Analysis of digestates was performed on an Agilent 7900 ICP-MS. Analytes were analyzed in the He collision cell mode to reduce polyatomic interferences. Samples and standards were diluted with a matrix of 2% HNO_3/0.5% HCl (v/v) (Fisher Scientific trace metal grade) made with 18.2 MΩ water. Prior to sample analysis, 97Mo, 120Sn, and 206 + 207 + 208Pb analytes were calibrated with single source Mo, Sn, and Pb (Spex Certiprep). Isotopes 89Y, 103Rh, 115In, and 209 Bi were used as internal standards to correct for shifts in the analyte signal intensity during the analysis run. NIST traceable second source standards were used to verify the calibration (High Purity Standards (CRM-TMDW-A): Pb,Mo, and Agilent: Sn).

TOF-SIMS for 2D Imaging and 3D Tomography. An ION-TOF TOF-SIMS V spectrometer was utilized for depth profiling and chemical imaging of the perovskite utilizing methods covered in detail in previous reports.[58] Analysis was completed utilizing a 3-lens 30 kV BiMn primary ion gun. High mass resolution depth profiles were completed with a 30 keV Bi_3^+ primary ion beam (1 pA pulsed beam current); a 50 μm × 50 μm area was analyzed with a 128:128 primary beam raster. 3-D Tomography and high-resolution imaging were completed with a 30 keV Bi_3^{2+} primary ion beam (0.1 pA pulsed beam current); a 50 μm × 50 μm area was analyzed with a 512:512 primary beam raster. In both cases, the primary ion beam dose density was kept below 1×10^{12} ions cm^{-2} to remain under the static-SIMS limit. Sputter depth profiling was accomplished with 1 kV Cesium ion beam (6 nA sputter current) with a raster of 150 × 150 μm.

TOF-SIMS for Fluorine Quantification. ToF-SIMS analyses were conducted using a TOF SIMS V (ION TOF, Inc. Chestnut Ridge, NY) instrument equipped with a Bi_n^{m+} (n = 1−5, m = 1, 2) liquid metal ion gun, Cs^+ sputtering gun, and electron flood gun for charge compensation. Both the Bi and Cs ion columns are oriented at 45° with respect to the sample surface normal. The instrument vacuum system consists of a load lock for rapid sample loading and an analysis chamber, separated by the gate valve. The analysis chamber pressure is maintained below 5.0×10^{-9} mbar to avoid contamination of the surfaces to be analyzed. For depth profiles acquired in this study, 3 keV Cs^+ with 5 nA current was used to create a 170 μm by 170 μm area, and the middle 50 μm by 50 μm area was analyzed using 0.3 pA Bi_3^+ primary ion beam. The negative secondary ion mass spectra were calibrated using O^-, F^- PbI_2^-, SnI_2^-.

Dark Hall Measurement. A Parallel Dipole Line (PDL) Hall system (PDL-1000 from Semilab) was employed to produce a unidirectional, pure single harmonic AC magnetic field with a peak-to-peak value of approximately 4 T (approximately ± 2 T from the center). This field was monitored by a Hall sensor.[59] The system is designed for high sensitivity, capable of handling mobility values less than 0.1 $cm^2/(V\,s)$, and ensures uniformity (<2%) for sample sizes up to 10 mm × 10 mm. The traditional Hall-bar geometry was utilized, and prior to conducting Hall measurements, current−voltage (I−V) tests were performed to verify contact quality. Subsequently, dark Hall measurements were carried out, with Figures S2−S4 providing examples of undoped, F_4TCNQ-doped, and $Mo(tfd\text{-}COCF_3)_3$-doped $MAPb_{0.5}Sn_{0.5}I_3$ film responses. Hall measurements were conducted using two configurations. For both configurations, the current was applied between terminals 2 and 5 (Figure S12), with voltage measured between terminals 4 and 6 in the first configuration, and between terminals 1 and 3 in the second configuration. Results from both were normally used for analysis. However, when one configuration produced unclear signals, likely due to contact issues, only the results from the remaining configuration were considered. A Fourier spectral analysis of the Hall resistance, following polynomial background subtraction, was conducted to identify the Hall signal frequency matching the reference oscillating magnetic field (Figures S2−S4). The signal processing and user interface software provided by Semilab facilitated software-controlled measurement and automated parameter extraction. Software lock-in detection with a time constant of 30 s was performed to extract the final Hall signal from the raw Hall resistance data (Figures S2−S4).

To calculate conductivity (σ), resistivity was measured in the 6-terminal Hall bar device. For the measurement, the current (I) was measured along the length of the device (i.e., between terminals 2 and 5) and the voltage (V) was measured across adjacent terminals (e.g., terminal 6 and 1) (Figure S12). The sheet resistance is calculated as $R_s = V/I$ and resistivity (ρ) is then determined using $\rho = R_s \cdot t$, where t is the sample thickness (270 nm). Conductivity is derived from

https://doi.org/10.1021/acsami.5c19800
ACS Appl. Mater. Interfaces XXXX, XXX, XXX−XXX

resistivity using $\sigma = 1/\rho$. For determining doping-dependent carrier properties, we ultimately analyzed only runs in which the control (undoped) samples (prepared for each independent run) showed consistent and low carrier density, for example remaining in the range of 10^{14}–10^{15} cm^{-3} (as determined by Hall measurements); thus, we can exclude the possibility that the shift in carrier density (and conductivity) with doping arises extraneously from sample exposure to oxygen.

X-ray Photoelectron Spectroscopy (XPS). XPS analyses were conducted using a Thermo Scientific Nexsa G2 instrument. Samples were transferred to the XPS system using a vacuum transfer holder to prevent exposure to air. To avoid influencing doping characteristics, samples were analyzed as introduced without etching. XPS spectra were collected using a monochromated, microfocused, low-power Al K-α X-ray source. All spectral data were calibrated relative to the C–C peak at 284.8 (±0.08) eV.

■ ASSOCIATED CONTENT

Supporting Information

The Supporting Information is available free of charge at https://pubs.acs.org/doi/10.1021/acsami.5c19800.

UV–vis measurement of F_4TCNQ and Mo(tfd-$COCF_3$)$_3$; Dark Hall measurement result graphs for an undoped $MAPb_{0.5}Sn_{0.5}I_3$ thin film; Dark Hall measurement result graphs for a F_4TCNQ-doped $MAPb_{0.5}Sn_{0.5}I_3$ thin film; Dark Hall measurement result graphs for a Mo(tfd-$COCF_3$)$_3$-doped $MAPb_{0.5}Sn_{0.5}I_3$ thin film; Film thickness of undoped, F_4TCNQ-doped (1×10^{-3} M), and Mo(tfd-$COCF_3$)$_3$-doped (1×10^{-3} M) $MAPb_{0.5}Sn_{0.5}I_3$ thin films; ICP spectroscopy measurement for Mo quantification; TOF-SIMS depth profiling of F_4TCNQ-doped and Mo(tfd-$COCF_3$)$_3$-doped $MAPb_{0.5}Sn_{0.5}I_3$ films; TOF-SIMS for fluorine and silicon signal detection from Mo(tfd-$COCF_3$)$_3$-doped $MAPb_{0.5}Sn_{0.5}I_3$ thin film; TOF-SIMS depth profiling for fluorine analysis using negative ion detection on undoped $MAPb_{0.5}Sn_{0.5}I_3$ films and bare glass substrates; TOF-SIMS depth profiling for fluorine semiquantification fromF_4TCNQ-doped and Mo(tfd-$COCF_3$)$_3$-doped $MAPb_{0.5}Sn_{0.5}I_3$ films, measuring negative ions (graph and summary table); Summary of doping efficiency calculations; X-ray photoelectron spectroscopy (XPS) analysis, with full scan spectrum of undoped, F_4TCNQ-doped, and Mo(tfd-$COCF_3$)$_3$-doped $MAPb_{0.5}Sn_{0.5}I_3$ thin films; High-resolution XPS spectra of Sn 3d, Pb 4f, and I 3d core levels for undoped, Mo(tfd-$COCF_3$)$_3$-doped, and F_4TCNQ-doped $MAPb_{0.5}Sn_{0.5}I_3$ films; Average binding energies (eV) and standard deviations obtained from independent XPS runs on undoped, Mo(tfd-$COCF_3$)$_3$-doped, and F_4TCNQ-doped perovskite films; 6-terminal Hall bar device configuration (PDF)

■ AUTHOR INFORMATION

Corresponding Author

David B. Mitzi – *Department of Mechanical Engineering and Materials Science, Duke University, Durham, North Carolina 27708, United States; Department of Chemistry, Duke University, Durham, North Carolina 27708, United States;* orcid.org/0000-0001-5189-4612; Email: david.mitzi@duke.edu

Authors

Migon Choi – *Department of Mechanical Engineering and Materials Science, Duke University, Durham, North Carolina 27708, United States*

Nelson Rivera – *Department of Civil & Environmental Engineering, Duke University, Durham, North Carolina 27708, United States*

Steven P. Harvey – *National Renewable Energy Laboratory, Golden, Colorado 80401, United States;* orcid.org/0000-0001-6120-7062

Chuanzhen Zhou – *Analytical Instrumentation Facility, North Carolina State University, Raleigh, North Carolina 27695, United States*

Sameera Pathiranage – *Analytical Instrumentation Facility, North Carolina State University, Raleigh, North Carolina 27695, United States;* orcid.org/0009-0002-7281-0646

Yadong Zhang – *Renewable & Sustainable Energy Institute, University of Colorado Boulder, Boulder, Colorado 80309, United States*

Stephen Barlow – *Renewable & Sustainable Energy Institute, University of Colorado Boulder, Boulder, Colorado 80309, United States;* orcid.org/0000-0001-9059-9974

Seth R. Marder – *Renewable & Sustainable Energy Institute, University of Colorado Boulder, Boulder, Colorado 80309, United States; Department of Chemical and Biological Engineering and Department of Chemistry, University of Colorado Boulder, Boulder, Colorado 80309, United States*

Complete contact information is available at: https://pubs.acs.org/10.1021/acsami.5c19800

Notes

The authors declare no competing financial interest.

■ ACKNOWLEDGMENTS

This work was primarily supported by the National Science Foundation under award number DMR-2004869. The synthesis of Mo(tfd-$COCF_3$)$_3$ was supported by the National Science Foundation through the DMREF program (DMR-1729737). Contributions of SB and SRM to data interpretation and manuscript editing were supported through the Center for Hybrid Organic Inorganic Semiconductors for Energy (CHOISE), an Energy Frontier Research Center (EFRC) funded by the Office of Basic Energy Sciences, Office of Science within the U.S. Department of Energy. This work was authored in part by the National Renewable Energy Laboratory, operated by Alliance for Sustainable Energy, LLC, for the U.S. Department of Energy (DOE) under Contract No. DE-AC36-08GO28308. We acknowledge Dr. Carrie Donley's insights on XPS interpretation. The views expressed in the article do not necessarily represent the views of the DOE or the U.S. Government. The U.S. Government retains and the publisher, by accepting the article for publication, acknowledges that the U.S. Government retains a nonexclusive, paid-up, irrevocable, worldwide license to publish or reproduce the published form of this work, or allow others to do so, for U.S. Government purposes.

■ REFERENCES

(1) Chen, Q.; Luo, J.; He, R.; Lai, H.; Ren, S.; Jiang, Y.; Wan, Z.; Wang, W.; Hao, X.; Wang, Y.; Zhang, J.; Constantinou, I.; Wang, C.; Wu, L.; Fu, F.; Zhao, D. Unveiling Roles of Tin Fluoride Additives in High-Efficiency Low-Bandgap Mixed Tin-Lead Perovskite Solar Cells. *Adv. Energy Mater.* **2021**, *11*, No. 2101045.

(2) Li, C.; Song, Z.; Chen, C.; Xiao, C.; Subedi, B.; Harvey, S. P.; Shrestha, N.; Subedi, K. K.; Chen, L.; Liu, D.; Li, Y.; Kim, Y.-W.; Jiang, C.-S.; Heben, M. J.; Zhao, D.; Ellingson, R. J.; Podraza, N. J.; Al-Jassim, M.; Yan, Y. Low-Bandgap Mixed Tin−Lead Iodide Perovskites with Reduced Methylammonium for Simultaneous Enhancement of Solar Cell Efficiency and Stability. *Nat. Energy* **2020**, *5* (10), 768−776.
(3) Wang, C.; Song, Z.; Li, C.; Zhao, D.; Yan, Y. Low-Bandgap Mixed Tin-Lead Perovskites and Their Applications in All-Perovskite Tandem Solar Cells. *Adv. Funct. Mater.* **2019**, *29* (47), No. 1808801.
(4) Leijtens, T.; Prasanna, R.; Bush, K. A.; Eperon, G. E.; Raiford, J. A.; Gold-Parker, A.; Wolf, E. J.; Swifter, S. A.; Boyd, C. C.; Wang, H.-P.; Toney, M. F.; Bent, S. F.; McGehee, M. D. Tin−Lead Halide Perovskites with Improved Thermal and Air Stability for Efficient All-Perovskite Tandem Solar Cells. *Sustainable Energy Fuels* **2018**, *2* (11), 2450−2459.
(5) Liu, F.; Liu, K.; Rafique, S.; Xu, Z.; Niu, W.; Li, X.; Wang, Y.; Deng, L.; Wang, J.; Yue, X.; Li, T.; Wang, J.; Ayala, P.; Cong, C.; Qin, Y.; Yu, A.; Chi, N.; Zhan, Y. Highly Efficient and Stable Self-Powered Mixed Tin-Lead Perovskite Photodetector Used in Remote Wearable Health Monitoring Technology. *Adv. Sci.* **2023**, *10* (5), No. 2205879.
(6) Qiu, W.; Xiao, Z.; Roh, K.; Noel, N. K.; Shapiro, A.; Heremans, P.; Rand, B. P. Mixed Lead−Tin Halide Perovskites for Efficient and Wavelength-Tunable Near-Infrared Light-Emitting Diodes. *Adv. Mater.* **2019**, *31* (3), No. 1806105.
(7) Lin, R.; Xiao, K.; Qin, Z.; Han, Q.; Zhang, C.; Wei, M.; Saidaminov, M. I.; Gao, Y.; Xu, J.; Xiao, M.; Li, A.; Zhu, J.; Sargent, E. H.; Tan, H. Monolithic All-Perovskite Tandem Solar Cells with 24.8% Efficiency Exploiting Comproportionation to Suppress Sn(II) Oxidation in Precursor Ink. *Nat. Energy* **2019**, *4* (10), 864−873.
(8) Hu, S.; Otsuka, K.; Murdey, R.; Nakamura, T.; Truong, M. A.; Yamada, T.; Handa, T.; Matsuda, K.; Nakano, K.; Sato, A.; Marumoto, K.; Tajima, K.; Kanemitsu, Y.; Wakamiya, A. Optimized Carrier Extraction at Interfaces for 23.6% Efficient Tin−Lead Perovskite Solar Cells. *Energy Environ. Sci.* **2022**, *15* (5), 2096−2107.
(9) Xu, F.; Aydin, E.; Liu, J.; Ugur, E.; Harrison, G. T.; Xu, L.; Vishal, B.; Yildirim, B. K.; Wang, M.; Ali, R.; et al. Monolithic Perovskite/Perovskite/Silicon Triple-Junction Solar Cells with Cation double Displacement Enabled 2.0 eV Perovskites. *Joule* **2024**, *8* (1), 224−240.
(10) Liu, H.; Wang, L.; Li, R.; Shi, B.; Wang, P.; Zhao, Y.; Zhang, X. Modulated Crystallization and Reduced V_{OC} Deficit of Mixed Lead−Tin Perovskite Solar Cells with Antioxidant Caffeic Acid. *ACS Energy Lett.* **2021**, *6* (8), 2907−2916.
(11) Xiao, K.; Lin, R.; Han, Q.; Hou, Y.; Qin, Z.; Nguyen, H. T.; Wen, J.; Wei, M.; Yeddu, V.; Saidaminov, M. I.; Gao, Y.; Luo, X.; Wang, Y.; Gao, H.; Zhang, C.; Xu, J.; Zhu, J.; Sargent, E. H.; Tan, H. All-Perovskite Tandem Solar Cells with 24.2% Certified Efficiency and Area over 1 cm^2 Using Surface-Anchoring Zwitterionic Antioxidant. *Nat. Energy* **2020**, *5* (11), 870−880.
(12) Kim, H.; Lee, J. W.; Han, G. R.; Kim, S. K.; Oh, J. H. Synergistic Effects of Cation and Anion in an Ionic Imidazolium Tetrafluoroborate Additive for Improving the Efficiency and Stability of Half-Mixed Pb-Sn Perovskite Solar Cells. *Adv. Funct. Mater.* **2021**, *31* (11), No. 2008801.
(13) Zhu, Z.; Li, N.; Zhao, D.; Wang, L.; Jen, A. K. Y. Improved Efficiency and Stability of Pb/Sn Binary Perovskite Solar Cells Fabricated by Galvanic Displacement Reaction. *Adv. Energy Mater.* **2019**, *9* (7), No. 1802774.
(14) Jiang, T.; Chen, Z.; Chen, X.; Liu, T.; Chen, X.; Sha, W. E. I.; Zhu, H.; Yang, Y. Realizing High Efficiency over 20% of Low-Bandgap Pb−Sn-Alloyed Perovskite Solar Cells by In Situ Reduction of Sn^{4+}. *Solar RRL* **2020**, *4* (3), No. 1900467.
(15) Zhou, X.; Peng, W.; Liu, Z.; Zhang, Y.; Zhang, L.; Zhang, M.; Liu, C.; Yan, L.; Wang, X.; Xu, B. Additive engineering with 2,8-dibromo-dibenzothiophene-S,S-dioxide enabled tin-based perovskite solar cells with 14.98% power conversion efficiency. *Energy Environ. Sci.* **2024**, *17* (8), 2837−2844.
(16) Liu, C.; Li, W.; Li, H.; Zhang, C.; Fan, J.; Mai, Y. C60 additive-assisted crystallization in $CH_3NH_3Pb_{0.75}Sn_{0.25}I_3$ perovskite solar cells with high stability and efficiency. *Nanoscale* **2017**, *9* (37), 13967−13975.
(17) Zhou, J.; Fu, S.; Zhou, S.; Huang, L.; Wang, C.; Guan, H.; Pu, D.; Cui, H.; Wang, C.; Wang, T.; Meng, W.; Fang, G.; Ke, W. Mixed Tin-Lead Perovskites with Balanced Crystallization and Oxidation Barrier for All-Perovskite Tandem Solar Cells. *Nat. Commun.* **2024**, *15* (1), No. 2324.
(18) Zhang, Z.; Liang, J.; Wang, J.; Zheng, Y.; Wu, X.; Tian, C.; Sun, A.; Chen, Z.; Chen, C.-C. Resolving Mixed Intermediate Phases in Methylammonium-Free Sn−Pb Alloyed Perovskites for High-Performance Solar Cells. *Nano-Micro Lett.* **2022**, *14* (1), 165.
(19) Hu, M.; Chen, M.; Guo, P.; Zhou, H.; Deng, J.; Yao, Y.; Jiang, Y.; Gong, J.; Dai, Z.; Zhou, Y.; Qian, F.; Chong, X.; Feng, J.; Schaller, R. D.; Zhu, K.; Padture, N. P.; Zhou, Y. Sub-1.4eV Bandgap Inorganic Perovskite Solar Cells with Long-Term Stability. *Nat. Commun.* **2020**, *11* (1), No. 151.
(20) Noel, N. K.; Habisreutinger, S. N.; Pellaroque, A.; Pulvirenti, F.; Wenger, B.; Zhang, F.; Lin, Y.-H.; Reid, O. G.; Leisen, J.; Zhang, Y.; Barlow, S.; Marder, S. R.; Kahn, A.; Snaith, H. J.; Arnold, C. B.; Rand, B. P. Interfacial Charge-Transfer Doping of Metal Halide Perovskites for High Performance Photovoltaics. *Energy Environ. Sci.* **2019**, *12* (10), 3063−3073.
(21) Rajagopal, A.; Liang, P.-W.; Chueh, C.-C.; Yang, Z.; Jen, A. K. Y. Defect Passivation via a Graded Fullerene Heterojunction in Low-Bandgap Pb−Sn Binary Perovskite Photovoltaics. *ACS Energy Lett.* **2017**, *2* (11), 2531−2539.
(22) Cai, F.; Yan, Y.; Yao, J.; Wang, P.; Wang, H.; Gurney, R. S.; Liu, D.; Wang, T. Ionic Additive Engineering Toward High-Efficiency Perovskite Solar Cells with Reduced Grain Boundaries and Trap Density. *Adv. Funct. Mater.* **2018**, *28* (34), No. 1801985.
(23) Kiermasch, D.; Rieder, P.; Tvingstedt, K.; Baumann, A.; Dyakonov, V. Improved Charge Carrier Lifetime in Planar Perovskite Solar Cells by Bromine Doping. *Sci. Rep.* **2016**, *6* (1), No. 39333.
(24) Liang, C.; Zhao, D.; Li, P.; Wu, B.; Gu, H.; Zhang, J.; Goh, T. W.; Chen, S.; Chen, Y.; Sha, Z.; Shao, G.; Sum, T. C.; Xing, G. Simultaneously Boost Diffusion Length and Stability of Perovskite for High Performance Solar Cells. *Nano Energy* **2019**, *59*, 721−729.
(25) Zhang, X.; Liang, Q.; Song, Q.; Liu, Y.; Wang, Y.; Chen, Y.; Li, D.; Huang, W. Electrical Doping Regulation of Carrier Recombination Enhances the Perovskite Solar Cell Efficiency beyond 28%. *J. Phys. Chem. Lett.* **2024**, *15* (45), 11224−11233.
(26) Schramm, T.; Deconinck, M.; Ji, R.; Siliavka, E.; Hofstetter, Y. J.; Löffler, M.; Shilovskikh, V. V.; Brunner, J.; Li, Y.; Bitton, S.; Tessler, N.; Vaynzof, Y. Electrical Doping of Metal Halide Perovskites by Co-Evaporation and Application in PN Junctions. *Adv. Mater.* **2024**, *36* (29), No. 2314289.
(27) Shi, J.; Li, Y.; Li, Y.; Li, D.; Luo, Y.; Wu, H.; Meng, Q. From Ultrafast to Ultraslow: Charge-Carrier Dynamics of Perovskite Solar Cells. *Joule* **2018**, *2* (5), 879−901.
(28) Peng, J.; Chen, Y.; Zheng, K.; Pullerits, T.; Liang, Z. Insights into Charge Carrier Dynamics in Organo-Metal Halide Perovskites: From Neat Films to Solar Cells. *Chem. Soc. Rev.* **2017**, *46* (19), 5714−5729.
(29) Yang, B.; Han, K. Charge-Carrier Dynamics of Lead-Free Halide Perovskite Nanocrystals. *Acc. Chem. Res.* **2019**, *52* (11), 3188−3198.
(30) Euvrard, J.; Yan, Y.; Mitzi, D. B. Electrical Doping in Halide Perovskites. *Nat. Rev. Mater.* **2021**, *6* (6), 531−549.
(31) Euvrard, J.; Gunawan, O.; Zhong, X.; Harvey, S. P.; Kahn, A.; Mitzi, D. B. P-Type Molecular Doping by Charge Transfer in Halide Perovskite. *Mater. Adv.* **2021**, *2* (9), 2956−2965.
(32) Li, X.; Du, X.; Zhao, J.; Lin, H.; Zheng, C.; Tao, S. Layer-by-Layer Solution Processing Method for Organic Solar Cells. *Solar RRL* **2021**, *5* (1), No. 2000592.
(33) Kiefer, D.; Kroon, R.; Hofmann, A. I.; Sun, H.; Liu, X.; Giovannitti, A.; Stegerer, D.; Cano, A.; Hynynen, J.; Yu, L.; Zhang, Y.; Nai, D.; Harrelson, T. F.; Sommer, M.; Moulé, A. J.; Kemerink, M.;

https://doi.org/10.1021/acsami.5c19800
ACS Appl. Mater. Interfaces XXXX, XXX, XXX−XXX

Marder, S. R.; McCulloch, I.; Fahlman, M.; Fabiano, S.; Müller, C. Double Doping of Conjugated Polymers with Monomer Molecular Dopants. *Nat. Mater.* **2019**, *18* (2), 149−155.
(34) Mohapatra, S. K.; Zhang, Y.; Sandhu, B.; Fonari, M. S.; Timofeeva, T. V.; Marder, S. R.; Barlow, S. Synthesis, Characterization, and Crystal Structures of Molybdenum Complexes of Unsymmetrical Electron-Poor Dithiolene Ligands. *Polyhedron* **2016**, *116*, 88−95.
(35) Ogomi, Y.; Morita, A.; Tsukamoto, S.; Saitho, T.; Fujikawa, N.; Shen, Q.; Toyoda, T.; Yoshino, K.; Pandey, S. S.; Ma, T.; Hayase, S. $CH_3NH_3Sn_xPb_{(1-x)}I_3$ Perovskite Solar Cells Covering up to 1060 nm. *J. Phys. Chem. Lett.* **2014**, *5* (6), 1004−1011.
(36) Gao, W.; Kahn, A. Electrical Doping: The Impact on Interfaces of π-Conjugated Molecular Films. *J. Phys.: Condens. Matter* **2003**, *15* (38), S2757−S2770.
(37) Belasco, J.; Mohapatra, S. K.; Zhang, Y.; Barlow, S.; Marder, S. R.; Kahn, A. Molecular Doping and Tuning Threshold Voltage in 6,13-Bis(Triisopropylsilylethynyl)Pentacene/Polymer Blend Transistors. *Appl. Phys. Lett.* **2014**, *105* (6), No. 063301.
(38) Wu, J.; Zhang, Y.; Yang, S.; Chen, Z.; Zhu, W. Thin $MAPb_{0.5}Sn_{0.5}I_3$ Perovskite Single Crystals for Sensitive Infrared Light Detection. *Front. Chem.* **2022**, *9*, No. 821699.
(39) Yurash, B.; Cao, D. X.; Brus, V. V.; Leifert, D.; Wang, M.; Dixon, A.; Seifrid, M.; Mansour, A. E.; Lungwitz, D.; Liu, T.; Santiago, P. J.; Graham, K. R.; Koch, N.; Bazan, G. C.; Nguyen, T.-Q. Towards Understanding the Doping Mechanism of Organic Semiconductors by Lewis Acids. *Nat. Mater.* **2019**, *18* (12), 1327−1334.
(40) Dixon, A. L.; Vezin, H.; Nguyen, T.-Q.; Reddy, G. N. M. Structural Insights into Lewis Acid- and F_4TCNQ-Doped Conjugated Polymers by Solid-State Magnetic Resonance Spectroscopy. *Materials Horizons* **2022**, *9* (3), 981−990.
(41) Cao, K.; Zhu, J.; Wu, Y.; Ge, M.; Zhu, Y.; Qian, J.; Wang, Y.; Hu, K.; Lu, J.; Shen, W.; Liu, L.; Chen, S. Suppressing Excess Lead Iodide Aggregation and Reducing N-Type Doping at Perovskite/HTL Interface for Efficient Perovskite Solar Cells. *Small* **2023**, *19* (43), No. 2301822.
(42) Euvrard, J.; Pournia, S.; Gunawan, O.; Mitzi, D. B. Giant Persistent Photoconductivity at Room Temperature in Sn-Based Perovskites. *Appl. Phys. Lett.* **2025**, *126* (6), No. 063302.
(43) Farvacque, J.-L.; Bougrioua, Z. Carrier Mobility Versus Carrier Density in $Al_xGa_{1-x}N$/GaN Quantum Wells. *Phys. Rev. B* **2003**, *68* (3), 15.
(44) Pachoud, A.; Jaiswal, M.; Ang, P. K.; Loh, K. P.; Özyilmaz, B. Graphene Transport at High Carrier Densities Using a Polymer Electrolyte Gate. *Europhys. Lett.* **2010**, *92* (2), 27001.
(45) Gosling, J. H.; Makarovsky, O.; Wang, F.; Cottam, N. D.; Greenaway, M. T.; Patanè, A.; Wildman, R. D.; Tuck, C. J.; Turyanska, L.; Fromhold, T. M. Universal Mobility Characteristics of Graphene Originating from Charge Scattering by Ionised Impurities. *Commun. Phys.* **2021**, *4* (1), 30.
(46) Hao, F.; Stoumpos, C. C.; Chang, R. P. H.; Kanatzidis, M. G. Anomalous Band Gap Behavior in Mixed Sn and Pb Perovskites Enables Broadening of Absorption Spectrum in Solar Cells. *J. Am. Chem. Soc.* **2014**, *136* (22), 8094−8099.
(47) Salzmann, I.; Heimel, G.; Oehzelt, M.; Winkler, S.; Koch, N. Molecular Electrical Doping of Organic Semiconductors: Fundamental Mechanisms and Emerging Dopant Design Rules. *Acc. Chem. Res.* **2016**, *49* (3), 370−378.
(48) Wu, W.-Q.; Wang, Q.; Fang, Y.; Shao, Y.; Tang, S.; Deng, Y.; Lu, H.; Liu, Y.; Li, T.; Yang, Z.; Gruverman, A.; Huang, J. Molecular Doping Enabled Scalable Blading of Efficient Hole-Transport-Layer-Free Perovskite Solar Cells. *Nat. Commun.* **2018**, *9* (1), No. 1625.
(49) Haque, M. A.; Rosas Villalva, D.; Hernandez, L. H.; Tounesi, R.; Jang, S.; Baran, D. Role of Dopants in Organic and Halide Perovskite Energy Conversion Devices. *Chem. Mater.* **2021**, *33* (21), 8147−8172.
(50) Zhang, F.; Smith, H. L.; Kahn, A. Molecular Dopants: Tools to Control the Electronic Structure of Metal Halide Perovskite Interfaces. *Appl. Phys. Rev.* **2021**, *8* (4), No. 041301.
(51) Li, J.; Zhang, G.; Holm, D. M.; Jacobs, I. E.; Yin, B.; Stroeve, P.; Mascal, M.; Moulé, A. J. Introducing Solubility Control for Improved Organic P-Type Dopants. *Chem. Mater.* **2015**, *27* (16), 5765−5774.
(52) Kim, H.; Lee, J. W.; Han, G. R.; Kim, S. K.; Oh, J. H. Synergistic Effects of Cation and Anion in an Ionic Imidazolium Tetrafluoroborate Additive for Improving the Efficiency and Stability of Half-Mixed Pb-Sn Perovskite Solar Cells. *Adv. Funct. Mater.* **2021**, *31* (11), No. 2008801.
(53) Li, W.; Li, Z.; Zhou, S.; Gou, Y.; Li, G.; Li, J.; Wang, C.; Zeng, Y.; Yan, J.; Li, Y.; Dai, W.; Rong, Y.; Ke, W.; Wang, T.; Xu, H. Unveiling the Nexus between Irradiation and Phase Reconstruction in Tin-Lead Perovskite Solar Cells. *Nat. Commun.* **2025**, *16* (1), 506.
(54) Morgan, W. E.; Van Wazer, J. R. Binding Energy Shifts in the X-Ray Photoelectron Spectra of a Series of Related Group Iva Compounds. *J. Phys. Chem. A* **1973**, *77* (7), 964−969.
(55) Kim, J. H.; Oh, C. M.; Hwang, I. W.; Park, K.; Lee, K. Organic Surface Doping for High-Performance Perovskite Transistors. *Adv. Funct. Mater.* **2025**, *35* (2), No. 2411836.
(56) Cornwell, A. B.; Harrison, P. G.; Richards, J. A. Structural Studies in Main Group Chemistry: XIX. Organotin(IV) Derivatives of Tetracyanoethylene, 7,7,8,8-Tetracyanoquinodimethane and 2,3,5,6-Tetrachlorobenzoquinone. The Isolation of Stable Organotin-Substituted Radicals. *J. Organomet. Chem.* **1977**, *140* (3), 273−287.
(57) Paniagua, S. A.; Baltazar, J.; Sojoudi, H.; Mohapatra, S. K.; Zhang, S.; Henderson, C. L.; Graham, S.; Barlow, S.; Marder, S. R. Production of Heavily N- and P-Doped CVD Graphene with Solution-Processed Redox-Active Metal−Organic Species. *Mater. Horiz.* **2014**, *1* (1), 111−115.
(58) Harvey, S. P.; Messinger, J.; Zhu, K.; Luther, J. M.; Berry, J. J. Investigating the Effects of Chemical Gradients on Performance and Reliability within Perovskite Solar Cells with TOF-SIMS. *Adv. Energy Mater.* **2020**, *10* (26), No. 1903674.
(59) Gunawan, O.; Pae, S. R.; Bishop, D. M.; Virgus, Y.; Noh, J. H.; Jeon, N. J.; Lee, Y. S.; Shao, X.; Todorov, T.; Mitzi, D. B.; Shin, B. Carrier-Resolved Photo-Hall Effect. *Nature* **2019**, *575* (7781), 151−155.



https://doi.org/10.1021/acsami.5c19800
ACS Appl. Mater. Interfaces XXXX, XXX, XXX−XXX